Nanoscale

PAPER

View Article Online
View Journal | View Issue

Cite this: *Nanoscale*, 2014, **6**, 3585

A compressible mesoporous SiO_2 sponge supported by a carbon nanotube network†

Yanbing Yang,[ab] Enzheng Shi,[b] Peixu Li,[c] Dehai Wu,[c] Shiting Wu,[b] Yuanyuan Shang,[b] Wenjing Xu,[b] Anyuan Cao*[b] and Quan Yuan*[a]

Received 7th November 2013
Accepted 29th December 2013

DOI: 10.1039/c3nr05931f

www.rsc.org/nanoscale

Applications of mesoporous silica (m-SiO_2) have suffered from its fragility (monolithic m-SiO_2 easily collapses under compression) and limited internal molecular exchange through small channels. Previously reported hierarchical porous m-SiO_2 structures containing interconnected macropores could improve adsorption properties, but they were still intrinsically fragile without sufficient mechanical strength to sustain deformation. Here, we embed a three-dimensional carbon nanotube (CNT) skeleton into m-SiO_2 to fabricate bulk, robust sponges that can be compressed to large strains (60% volume reduction) repeatedly in both air and water. This is done by directly casting a uniform m-SiO_2 layer with tunable thickness onto the surface of CNTs while maintaining the original network and open porous structure, resulting in a core–shell CNT@m-SiO_2 hybrid sponge. By pumping fluid through the CNT@m-SiO_2 sponges under cyclic compression, the adsorption rate and efficiency of dye molecules can be significantly enhanced due to the mesoporous coating on CNTs and enhanced fluid exchange throughout internal pores. The CNT@m-SiO_2 sponges may be used as robust and flexible adsorption media, and chemical and biological sensors with high performance.

Introduction

Mesoporous silica (m-SiO_2) materials are lightweight and highly porous, with potential applications in many areas such as molecular adsorption, catalysis, gas and biological sensors.[1–6] Monolithic m-SiO_2 contains long-range ordered pores with uniform size and high surface area, and its large-area, open-pore surface is suitable for anchoring particles, trapping molecules, fast transport and optical manipulation.[7–15] However, such a highly ordered mesoporous structure also caused potential problems toward practical applications, in particular, the structure instability and limited diffusion process through narrow channels. During synthesis and subsequent treatments, bulk m-SiO_2 tends to crack and shrink, and the monolith easily collapses under small external stress or deformation. Second, molecular diffusion and mass transportation inside the m-SiO_2 monoliths, which are important processes related to adsorption and sensor applications, are limited by the mesoporous channels. In addition to powder form m-SiO_2, hierarchical porous structures containing both mesopores and macropores have been synthesized using swelling agents or templates such as a colloidal crystal and polymeric foam.[7,16,17] Adsorption properties are improved due to the presence of interconnected macropores, however, these m-SiO_2 foams consisting of aggregated particles or thin mesoporous walls are still inherently fragile structures, and their mechanical behavior has not yet been studied. For monolithic m-SiO_2, improvement of its microstructure and related mechanical properties remains a grand challenge.

Carbon nanotubes (CNTs) and graphene sheets are nanostructures with outstanding mechanical strength and flexibility, and in recent work, they have been self-assembled into low density, porous materials such as CNTs or graphene-based foams, aerogels and sponges.[18–30] Our group has reported bulk CNT sponges consisting of a three-dimensional CNT network which can be deformed to arbitrary shapes and compressed to large strains with elastic recovery.[20] Combining this flexible CNT network with high surface area m-SiO_2 is a promising approach to develop novel porous composites with tailored microstructures and enhanced mechanical properties. The CNT networks also have advantages such as higher thermal and chemical stability, and minimized plastic deformation compared to conventional polymeric foams with big (sub-mm) pores and very thin walls.[15] In fact, m-SiO_2 has been coated onto individual multi-walled or single-walled CNTs by non-covalent bonding, forming a core–shell structure with a uniform m-SiO_2 layer.[31–34] Initially, the purpose of coating m-SiO_2 on CNTs (in

[a]*Key Laboratory of Analytical Chemistry for Biology and Medicine (Ministry of Education), College of Chemistry and Molecular Sciences, Wuhan University, Wuhan 430072, China. E-mail: yuanquan@whu.edu.cn*

[b]*Department of Materials Science and Engineering, College of Engineering, Peking University, Beijing 100871, P.R. China. E-mail: anyuan@pku.edu.cn*

[c]*Department of Mechanical Engineering, Tsinghua University, Beijing 100084, P.R. China*

† Electronic supplementary information (ESI) available. See DOI: 10.1039/c3nr05931f

powder form) was to obtain a better dispersion of CNTs in solution, rather than creating an integral hybrid structure.

Here, we report a CNT@m-SiO_2 sponge consisting of a three-dimensional CNT network uniformly coated by m-SiO_2. The original CNT sponge serves as a porous template, and m-SiO_2 was directly cast onto the surface of CNTs through a solution process, with controlled layer thickness. Owing to the presence of a continuous CNT skeleton, the hybrid sponges are robust and flexible, and can be compressed to 60% strain without collapse. We demonstrate an application of these compressible CNT@m-SiO_2 sponges as a "pump" for dye removal from water, and show that pumping fluid through the internal pores significantly enhances the molecular adsorption efficiency.

Results and discussion

We adopted a sol–gel method to synthesize m-SiO_2 *in situ* within CNT sponge blocks, as illustrated in Fig. 1a and b. The idea is to coat a thin m-SiO_2 layer around all individual CNTs while maintaining their original network and porous structure. We therefore carried out the sol–gel process by infiltrating liquid precursors into the porous sponge, unlike previous reports where powder form CNTs were dispersed in solution by sonication.[31–34] A key issue here is to ensure that sufficient amounts of precursors access the internal part of the sponge and produce uniform m-SiO_2 layers throughout the CNT network. To do this, the precursor solution was dropped and sucked by the sponge, extruded after a certain reaction period, and fresh solution was added again for multiple times (see Experimental for details). The CNT network immersed in precursor solution served as a substrate for nucleation and formation of m-SiO_2. By this way, a CNT sponge was converted to a CNT@m-SiO_2 sponge with the same macroscopic morphology and size, and the initial black surface changed to a grey color indicating successful coating of m-SiO_2 (Fig. 1c). After burning CNTs by high temperature calcination (650 °C in air), the remaining m-SiO_2 monolith maintained the original shape and a stable structure (Fig. 1c).

Conventional monolithic m-SiO_2 materials are typically very fragile and collapse easily under modest compression or deformation. Here, the CNT@m-SiO_2 sponges inherit high flexibility from the embedded CNT skeleton, being stable under repeated compression to large strains (up to 60%). This is seen

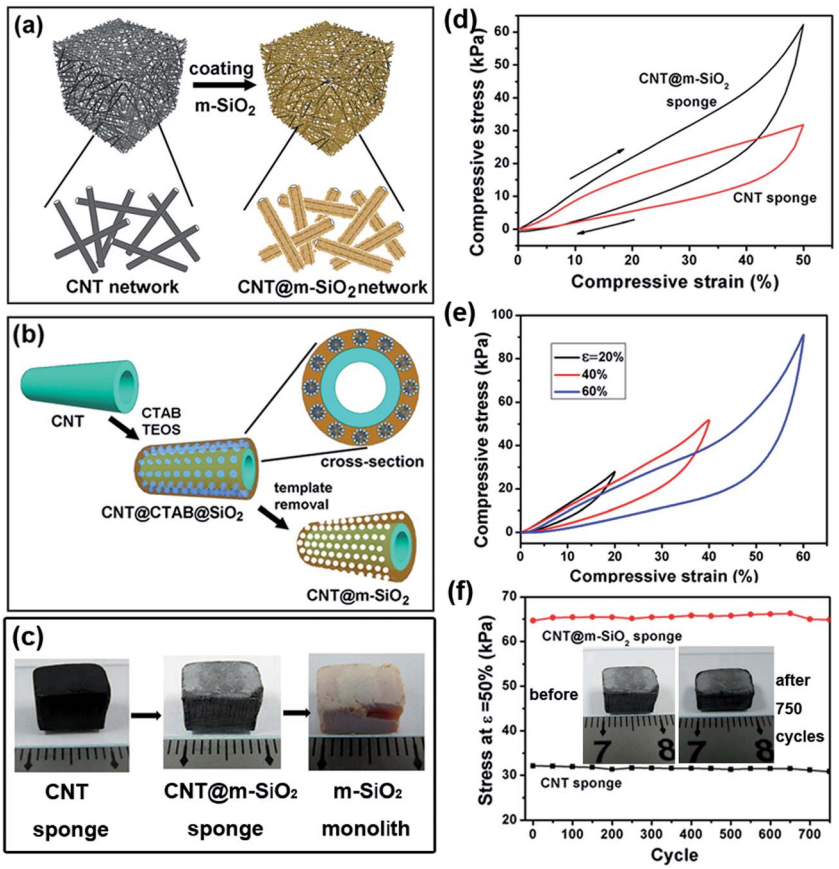

Fig. 1 Fabrication of CNT@m-SiO_2 sponges and mechanical properties. (a) Illustration of the structure of a CNT sponge and CNT@m-SiO_2 sponge after coating m-SiO_2 on the CNT network. (b) Synthesis procedure for the CNT@m-SiO_2 core–shell structures by the sol–gel method. (c) Photos of a bulk CNT and CNT@m-SiO_2 sponge, and a m-SiO_2 monolith after burning CNTs. Red color of the m-SiO_2 monolith is due to the residue Fe catalyst. (d) Compressive stress–strain curves of a CNT (10.46 × 8.40 × 5.50 mm^3) and CNT@m-SiO_2 (9.40 × 7.86 × 5.80 mm^3) sponge, respectively. Arrows point to loading and unloading directions. (e) Stress–strain curves of the CNT@m-SiO_2 sponge at different strains of 20%, 40%, and 60%, respectively. (f) Stress values at $\varepsilon = 50\%$ recorded over 750 cycles for the CNT and CNT@m-SiO_2 sponge, respectively. The inset shows photos of the CNT@m-SiO_2 sponge before and after 750 compression cycles.

from the compressive stress–strain (σ–ε) curves of a pristine CNT sponge and a CNT@m-SiO_2 hybrid sponge, with similar loops during loading and unloading stages (Fig. 1d). Compared to traditional monolithic m-SiO_2 materials, here the CNT network can sustain the entire structure during deformation, resulting in better compressibility. Furthermore, the hybrid sponge shows a higher compressive stress at $\varepsilon = 50\%$ ($\sigma \approx 62$ kPa) than the CNT sponge ($\sigma \approx 30$ kPa), indicating that the m-SiO_2 coating around individual nanotubes could reinforce the entire network structure. The strengthening effect is clearly evidenced from the gradually increasing compressive strength (from 52 to 160 kPa) with thicker m-SiO_2 (from 8 to 20 nm) (Fig. S1a†). The CNT@m-SiO_2 sponge is also elastic with complete volume recovery since the unloading curves return to the origin without residual strain at compressive strains of 40% or less (Fig. 1e). At a higher strain ($\varepsilon = 60\%$), a small plastic deformation (residual strain < 5%) has developed after unloading. Here, it is the underlying CNT network that sustains large deformation and enables elastic recovery, making the CNT@m-SiO_2 structure highly flexible and robust, which overcomes the inherent fragility of traditional m-SiO_2 monoliths. We have compressed the CNT@m-SiO_2 sponge to $\varepsilon = 50\%$ for 750 cycles and found no stress degradation, indicating fatigue resistance (Fig. 1f and ESI, Fig. S2†). Although the sponge thickness has reduced by about 15% after cyclic compression, the bulk porous structure is well maintained without breaking or forming cracks in the monolith (Fig. 1f).

The morphology and structure of CNT@m-SiO_2 sponges were characterized by scanning electron microscopy (SEM) and transmission electron microscopy (TEM) images. The CNTs at the sponge surface have been coated by m-SiO_2, and their average diameter increases from about 30 nm to 90 nm (m-SiO_2 thickness = 30 nm) (Fig. 2a). Most of the nanotube length is wrapped by m-SiO_2 while protruding nanotube ends are frequently observed, clearly showing the core–shell structure (Fig. 2b). Cross-sectional SEM images of the inner part show core–shell structures with 10 nm thick m-SiO_2 uniformly coated on CNTs (Fig. 2c). Compared with the outer surface in direct contact with precursors, the m-SiO_2 formed inside the sponge has a smaller thickness due to limited precursor amount within the pores, and the m-SiO_2 thickness is uniform (without gradient) throughout the monolith except for the outer surface. TEM images reveal uniform core–shell structures with a nanotube cavity and a mesoporous shell with a pore size of 2–5 nm (Fig. 2d and e). The m-SiO_2 thicknesses at the surface and inner parts of the sponge are about 30 nm and 10 nm, respectively, consistent with SEM images. Since the surfactant molecules are stacked on the CNT surface as a soft template to generate mesopores, this method could produce conformal and smooth m-SiO_2 layers with different thicknesses. The high resolution TEM image also shows an exposed CNT section in a m-SiO_2 crack (Fig. 2f).

It is important to produce a uniform m-SiO_2 layer with controlled thickness throughout the sponge. Two key factors here include (1) the weight ratio of cetyltrimethyl ammonium bromide (CTAB, relative to CNTs) which influences the pore formation and m-SiO_2 uniformity, and (2) the amount of

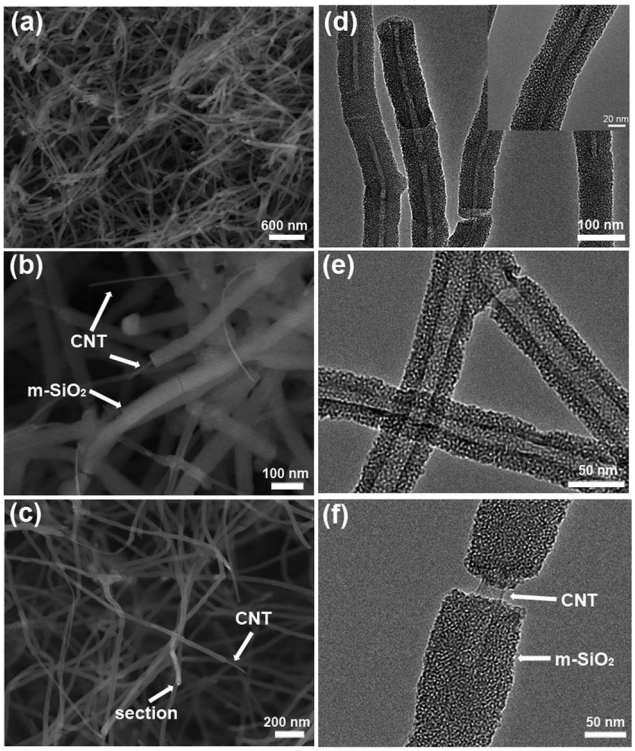

Fig. 2 Structure characterization of CNT@m-SiO_2 sponges. (a) SEM images of the outer surface showing uniform m-SiO_2 coating on the CNTs while maintaining the porous network structure. (b) Enlarged view showing core–shell CNT@m-SiO_2 structures, with some CNTs protruding from the ends. (c) SEM image of the inner part of the sponge, showing uniform but thinner m-SiO_2 coating on CNTs. (d) TEM image of the CNT@m-SiO_2 structures consisting of a CNT core and m-SiO_2 shell. Inset, HRTEM image of CNT@m-SiO_2 sponges, which clearly indicates the open pore structure and smooth coating on CNTs. (e) TEM image of the CNT@m-SiO_2 structures with a relatively thin m-SiO_2 layer. (f) High resolution TEM image of a core–shell CNT@m-SiO_2 structure in which the CNT exposes from the cracked region in the m-SiO_2 layer.

tetraethyl orthosilicate (TEOS) which determines the m-SiO_2 layer thickness. As the CTAB to CNT ratio increases from 2 : 1 to 30 : 1 (TEOS amount fixed at 0.05 g), the product morphology changes from nonporous SiO_2 (CTAB : CNT = 2 : 1) to irregular m-SiO_2 (10 : 1) and finally smooth m-SiO_2 (30 : 1) (Fig. S3†). On the other hand, increasing the TEOS amount from 0.03 to 0.07 g (for 15 mg sponge) could increase the m-SiO_2 shell thickness from 8 nm (TEOS = 0.03 g) to 13 nm (0.05 g), and then 20 nm (0.07 g) inside the sponge (Fig. S3†).

We have done comprehensive spectroscopic and thermal analysis to characterize the formation of m-SiO_2, its porous structure, interface with CNTs, and stability. The Fourier transform infrared (FTIR) spectra of the CNT sponge before and after reaction confirm the presence of m-SiO_2 within the sponge, as indicated by the absorption peak at 1094 cm^{-1} due to the Si–O–Si stretching vibration (Fig. 3a). X-ray photoelectron spectroscopy (XPS) characterization on the CNT sponge shows a pronounced C 1s peak, while in the CNT@m-SiO_2 sponge the C 1s peak intensity decreases substantially (Fig. 3b). At the same time, a strong O 1s peak and a Si 2p peak emerge after m-SiO_2

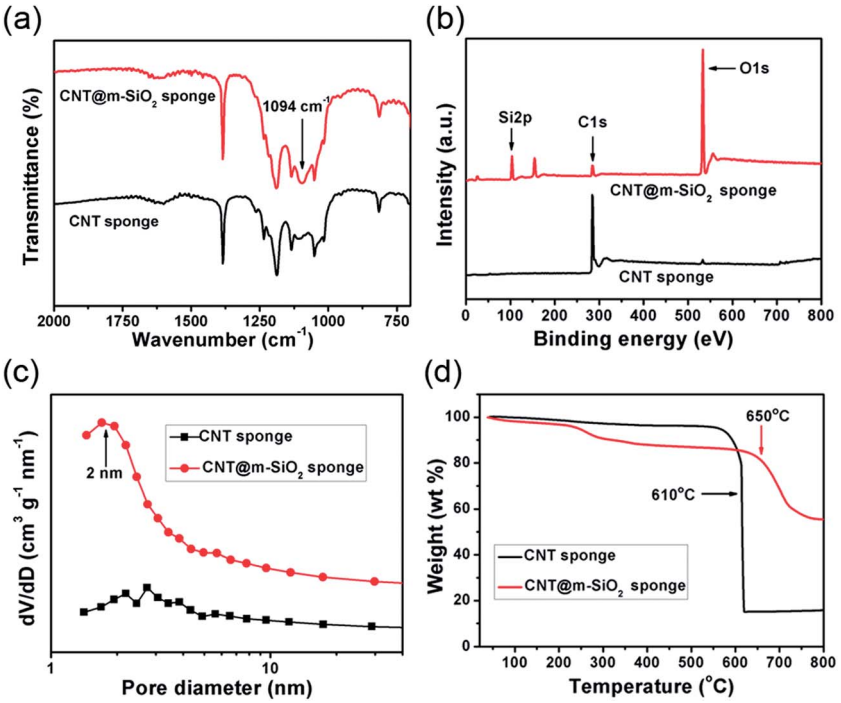

Fig. 3 Spectroscopy analysis and thermal stability. (a) FTIR spectra of the CNT and CNT@m-SiO_2 sponge. The spectra of the CNT@m-SiO_2 sponge are offset vertically for clarity. (b) XPS wide-scan spectra of the CNT and CNT@m-SiO_2 sponge; in the latter sample Si 2p and O 1s peaks emerge and the C 1s peak decreases. (c) Pore size distribution in the CNT and CNT@m-SiO_2 sponge. (d) TGA curves of the CNT and CNT@m-SiO_2 sponge heated in air from 30 to 800 °C.

coating. The pore structure and Brunauer–Emmett–Teller (BET) surface area are tested by N_2 adsorption–desorption isotherms. The isotherm after coating shows typical type IV curves due to the presence of cylindrical pores with a narrow size distribution at around 2 nm (Fig. S4a† and 3c), in agreement with TEM images. The original CNT sponge has a rather wide pore size range and a BET surface area of about 45 $m^2\ g^{-1}$. After m-SiO_2 coating, the surface area increases to 213 $m^2\ g^{-1}$ with a total pore volume of 0.27 $cm^3\ g^{-1}$. Initially, the CNT surface is very smooth. Now, the core–shell CNT@m-SiO_2 has a three-dimensional mesoporous surface, and also the space between CNTs is better utilized, resulting in increased surface area. For samples coated with other m-SiO_2 thicknesses such as 8 and 20 nm, their BET surface areas are also improved to 117 and 158 $m^2\ g^{-1}$, respectively (Fig. S1c†). The significant increase of surface area is due to introduction of a mesoporous layer (see high resolution TEM image in Fig. 2d, inset) within a macroporous CNT network, which is beneficial for applications such as catalysis and adsorption.

The CNT@m-SiO_2 interface is studied by Raman spectra. Both the CNT and CNT@m-SiO_2 sponges show characteristic bands at 1336 cm^{-1} (D-band) and 1575 cm^{-1} (G-band), which correspond to the disordered structure and C–C sp^2 bonding (E_{2g}) in graphitic sheets (Fig. S4b†). There is no significant band shift, and the intensity ratio between the D and G bands remains the same, indicating noncovalent interaction between the CNTs and the m-SiO_2 shell. In the CNT@m-SiO_2 core–shell structure, the inner CNT is shielded by the outside m-SiO_2 shell. X-ray diffraction (XRD) spectra show decreased (002) and (100) intensity due to this shielding effect (Fig. S4c†). Shielding CNTs with the m-SiO_2 shell also improves the thermal stability of the sponge, as proved by thermogravimetric analysis (TGA). The pristine CNT sponge has a combustion temperature at 610 °C in air, with about 15% of residue weight (oxidized iron catalyst) (Fig. 3d). In comparison, the CNT weight loss is delayed to a higher temperature (>650 °C) in the CNT@m-SiO_2 sponge under a 13 nm coating thickness. Here, the critical factor for enhancing the thermal stability is to coat m-SiO_2 uniformly throughout the monolith, realized by infiltration of precursors into the sponge pores during synthesis. The shielding effect is also proved by testing sponges with different m-SiO_2 thicknesses. The combustion of CNTs occurs at 630, 650, and 680 for sponges with 8, 13, and 20 nm m-SiO_2 coating, respectively. In the TGA curve of the CNT@m-SiO_2 sponge, there is a small weight loss at about 200 °C due to adsorbed water on silica. After burning CNTs, the remaining weight is about 50%, which approximates the initial m-SiO_2 loading into the sponge.

Our CNT@m-SiO_2 sponges contain both mesopores (from m-SiO_2) and interconnected macropores (space between CNTs), and this hierarchical porous structure is very suitable for adsorption applications. Since the CNT skeleton renders the sponge robust and compressible, we can adopt a dynamic adsorption mode—pumping liquid through the pores. For a bulk material, the simplest adsorption mode is to place it statically inside the solution and attract targeted molecules (methyl orange, MO) from around (Fig. 4a, inset). The adsorption process is monitored by spectroscopy measurements on the MO-water solution after a fixed period (*e.g.* 1 hour), for an

initial MO concentration of 0.02 mM and a sponge weight of 20 mg (see Experimental). In this static mode, we observe a gradual decrease in the intensity of the characteristic light absorption peak (465 nm) over a period of 10 hours, indicating continuous adsorption of MO molecules into the sponge (Fig. 4a). To realize dynamic adsorption, the sponge (immersed in solution) is compressed to 50% strain repeatedly in a mechanical testing instrument (Fig. S5†). We set a relatively slow compression rate on the sponge (about 100 cycles for a period of 10 hours) to enhance fluid exchange while minimizing disturbance to the solution. After 10 hours, the peak at 465 nm has completely disappeared indicating 100% adsorption of MO from the solution (Fig. 4b). From the spectroscopy curves of dye solutions adsorbed by a CNT sponge and a CNT@m-SiO_2 sponge (in static and dynamic modes, respectively) under the same conditions (sponge weight, initial MO concentration) (Fig. 4c), we can calculate and compare their adsorption efficiency (η), which is determined by $\eta = 1 - C_t/C_0$, where C_0 is the original dye concentration and C_t is the concentration after a certain adsorption period. After the same adsorption period (10 hours), the CNT sponge shows $\eta = 23.7\%$ and the MO peak at 465 nm remains strong. In comparison, the adsorption efficiency of the CNT@m-SiO_2 sponge reaches ~62.4% in static mode, and 100% in dynamic mode (Fig. 4d). Compressing sponges in the solution also improves the adsorption rate. It takes about 5 hours for a CNT@m-SiO_2 sponge to remove 50% dye concentration when it is placed in solution statically, whereas the adsorption period shortens to 1 hour for the same

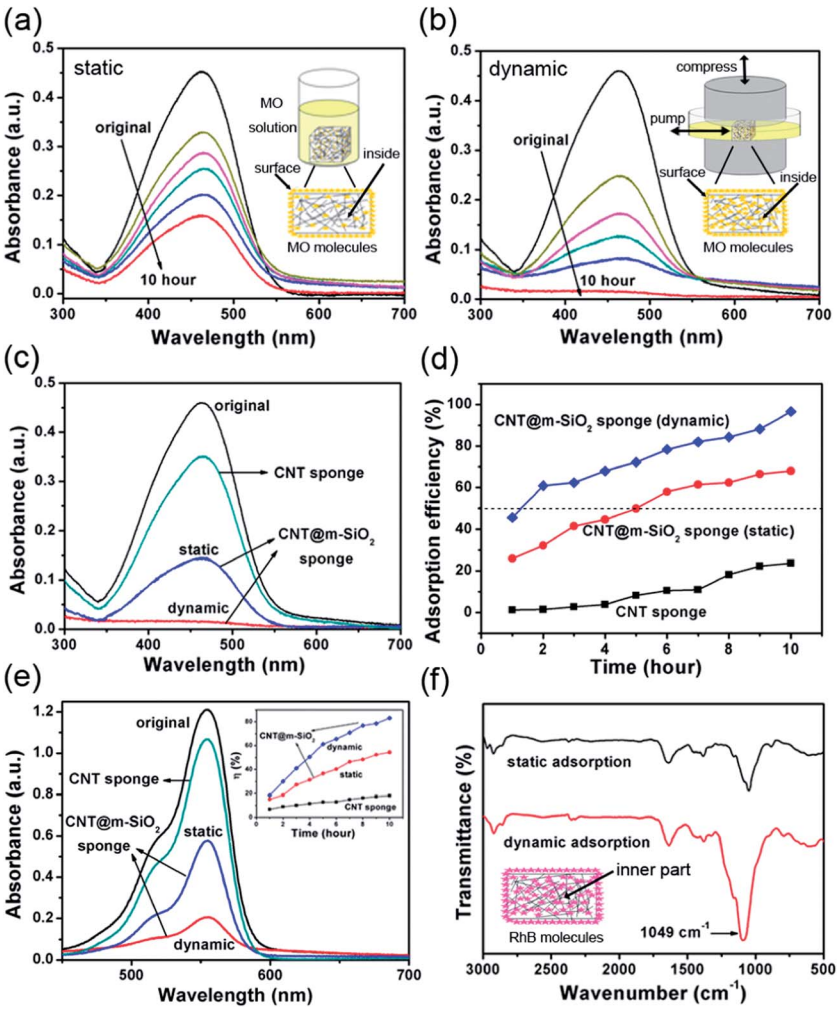

Fig. 4 Application in dye adsorption. (a) UV-Vis absorption spectra of a MO solution after different adsorption periods (2 hour interval until 10 hours) by a CNT@m-SiO_2 sponge under static conditions. The inset shows the adsorption setup in which the sponge was immersed in the solution. The dye adsorption in the inner part of the sponge is very limited. (b) UV-Vis absorption spectra by a CNT@m-SiO_2 sponge under dynamic conditions. The inset shows the setup in which the sponge was compressed cyclically during adsorption. The dye adsorption in the inner part is greatly enhanced. (c) UV-Vis spectra of MO solutions adsorbed (after 10 hours) by a CNT sponge, a CNT@m-SiO_2 sponge under static and dynamic conditions, respectively. (d) Calculated MO adsorption efficiencies of the CNT and CNT@m-SiO_2 sponge (static and dynamic) for different adsorption periods from 1 to 10 hours. The horizontal dashed line indicates adsorption of 50% dye amount (concentration). (e) UV-Vis spectra of RhB solutions after 10 hour adsorption by a CNT sponge, a CNT@m-SiO_2 sponge under static and dynamic conditions. The inset shows corresponding adsorption efficiencies. (f) FTIR spectra of the inner part of the CNT@m-SiO_2 sponge after adsorption of RhB under static and dynamic conditions.

sponge under cyclic compression. Significant improvement of the adsorption rate and efficiency is owing to (1) increased surface area by coating m-SiO_2 on CNTs and (2) the dynamic adsorption mode which enhances liquid exchange through the sponge pores by continuous pumping. Compared with the powder form, porous materials made in monolith have advantages such as easy handling and convenient recover, however, the diffusion process inside the bulk is limited by the small pores and narrow channels. Therefore it is imperative to enhance internal diffusion in monolithic porous structures during adsorption. Conventional m-SiO_2 monoliths are fragile, and there is no simple way to promote molecular adsorption into the inside pores. In contrast, our compressible CNT@m-SiO_2 sponges can serve as a pump to extrude solution out (by large-strain compressing) and uptake solution in (by releasing) to facilitate liquid exchange and molecular diffusion throughout the porous structure. By this way, the internal surface area provided by m-SiO_2 can be utilized maximally.

The mesopores in the m-SiO_2 layer have a pore size of about 2 nm matching the MO molecular size ($1.31 \times 0.55 \times 0.18$ nm^3), resulting in higher adsorption efficiency. To study the molecular size effect, we have tested another dye (rhodamine B, RhB) with a larger size ($1.59 \times 1.18 \times 0.56$ nm^3). Spectroscopic measurement on the characteristic peak at 554 nm shows that the adsorption efficiency of RhB reaches 83.1% after 10 hours (Fig. 4e), lower than MO (100%). The adsorption saturated amount for MO and RhB is 62.3 and 23.8 mg g^{-1}, respectively. The larger size of RhB molecules makes them difficult to enter the mesopores and mainly adsorb onto the m-SiO_2 surface, resulting in less available adsorption sites and decreased saturated amount compared with smaller MO molecules. On the other hand, similar to MO adsorption, the adsorption efficiency of RhB under dynamic compression is much higher than that under static conditions and pure CNT sponge (Fig. 4e, inset).

We have studied the mechanism underlying dynamic adsorption by characterizing the signal of RhB molecules adsorbed on the inner part of the sponge. After adsorption, the inner part of the sponge is examined by FTIR, which reveals a strong peak at 1049 cm^{-1} (C–N stretching vibration of RhB molecules), indicating that the inner part is also active for adsorption (Fig. 4f). In comparison, the peak intensity has decreased substantially after static adsorption. The results indicate that pumping fluid through the sponges (by cyclic compression) could facilitate molecular diffusion and adsorption to the internal area, and improve adsorption efficiency.

In conclusion, we fabricated CNT@m-SiO_2 sponges consisting of both macro- and mesopores by *in situ* coating a m-SiO_2 layer throughout the CNT network. In our hybrid sponges, the two components perform different functions. On one hand, the CNT network provides flexibility and compressibility; on the other hand, the m-SiO_2 layer provides higher surface area and also improves mechanical strength and thermal stability. Compared to traditional mesoporous silica monoliths, our sponges have a hierarchical pore structure and can be compressed to large strains for hundreds of cycles with elastic volume recovery. These compressible sponges can serve as a pump to promote fluid exchange through internal pores, with significantly enhanced adsorption efficiency for dye molecules. Robust, flexible mesoporous materials have many potential applications in energy and environmental areas.

Experimental materials and methods

Chemicals and materials

Cetyltrimethyl ammonium bromide (CTAB, ≥99.0%), tetraethyl orthosilicate (TEOS, ≥98.0%), ferrocene (≥98.0%) and 1,2-dichlorobenzene (≥99.0%) were purchased from Shanghai Chemical Corp. (Shanghai, China); ethanol (≥99.7%) and ammonia (25–28%) were provided by Beijing Fine Chemical Company. All chemicals were used as received without further purification. Millipore water was used in all experiments.

Fabrication of CNT@m-SiO_2 sponges

CNT sponges were synthesized by chemical vapor deposition using ferrocene and 1,2-dichlorobenzene as catalyst and carbon precursor, as described in our earlier report.[20] The core–shell CNT@m-SiO_2 sponges were fabricated by a sol–gel pathway[34] with some modifications. In a typical procedure, ~0.45 g of CTAB was dissolved into a mixture of 30 mL deionized water, 120 mL ethanol and 1.5 mL ammonia at room temperature. Subsequently, a mixture of the above solution (3 mL) and 0.05 g TEOS was dropped onto 15 mg CNT sponge in a glass Petri dish 8 times at 1 hour interval under continuous shaking. Finally, the sponge was added to a mixture of 0.4 g TEOS and the remaining solution containing water, ethanol and ammonia under magnetic stirring, and the reaction was processed at 50 °C for 24 h to ensure the sufficient coating of precursors on CNTs in the outer sponge surface. The mesoporous structure (m-SiO_2) was obtained *via* ion exchange between the CTAB surfactant and 0.01 M NH_4NO_3 in ethanol.

Sample characterization

TEM images were recorded on a FEI Tecnai G2 T20 (Tecnai T20) operated at 200 kV. The CNT@m-SiO_2 sponges for TEM characterization were dispersed in ethanol by sonication and separated core–shell structures were collected by copper grids for observation. SEM characterization was performed on a Hitachi S-4800 microscope (Hitachi, Japan). Raman spectra were collected on an RM 2000 Microscopic Confocal Raman Spectrometer (Renishaw PLC, England), using a He–Ne laser with an excitation wavelength of 633 nm. TGA analysis was carried out on a TGA Q5000 analyzer from 30 to 800 °C under air with a heating rate of 20 °C min^{-1}. Powder XRD patterns were recorded on a Bruker D8 diffractometer with Cu Kα adiation ($\lambda = 0.15418$ nm), in a 2θ range from 10 to 50° with a speed of 6° min^{-1}. Nitrogen sorption isotherms were measured at 77 K using a Quantachrome Autosorb-iQ analyzer. Before measurements, all of the samples were degassed in a vacuum at 100 °C for 10 h. The BET method was used to calculate the specific surface areas; the pore volume and pore size distribution were obtained using the Barrett–Joyner–Halenda (BJH) method. XPS measurements were performed using an ESCALAB 250Xi spectrometer. The UV-vis spectra were recorded on a Cary 5000 UV-Vis-NIR (Agilent) spectrometer to determine

the concentration of RhB and MO solutions. Fourier transform infrared spectra (FTIR, Nicolet iS10, THERMO, America) were used to characterize the transmission spectrum of samples. Mechanical measurements on CNT and CNT@m-SiO_2 sponges (compressive and tensile tests) were carried out using a single-column static instrument (Instron 5843) equipped with two flat compression stages and two load cells (10 N and 1 kN). Cyclic compression on sponges was performed at a set maximum strain (50%) for 750 cycles.

Dye adsorption experiments

The adsorption capacities of CNT and CNT@m-SiO_2 sponges were investigated using RhB and MO molecules, under static and dynamic conditions, respectively. Under static conditions, a bulk CNT or CNT@m-SiO_2 sponge (20 mg, 11.58 × 10.0 × 8.20 mm^3) was placed in a glass Petri dish and immersed in 10 mL RhB or MO solution (initial concentration of 0.02 mM). After a certain period (1 hour), a portion of the solution was picked up for UV-Vis measurement to determine the remaining dye concentration in the solution and calculate adsorption efficiency. For dynamic conditions, a bulk CNT@m-SiO_2 sponge (20 mg) was immersed in dye solution and simultaneously compressed by a compression stage installed in Instron 5843. The maximum strain was set as 50%, and the sponge was compressed at a strain rate of 20% per minute constantly during the entire adsorption process (10 hours). In each compression cycle, the solution was extruded out of the sponge during the loading stage and re-sucked into the sponge during unloading. The fluid exchange process is relatively smooth (without causing much disturbance) at such a low strain rate.

Acknowledgements

This work was supported by the National Science Foundation of China (NSFC, grant number 91127004, 21201133, 51272186) and the Beijing City Science and Technology Program (Z121100001312005). Q. Yuan thanks Wuhan University for start-up funds and thanks large-scale instrument and equipment sharing foundation of Wuhan University.

References

1 A. Taguchi and F. Schüth, Ordered Mesoporous Materials in Catalysis, *Microporous Mesoporous Mater.*, 2005, **77**, 1–45.
2 A. Corma, From Microporous to Mesoporous Molecular Sieve Materials and Their Use in Catalysis, *Chem. Rev.*, 1997, **97**, 2373–2419.
3 J. Fan, C. Z. Yu, F. Gao, J. Lei and D. Y. Zhao, Cubic Mesoporous Silica with Large Controllable Entrance Sizes and Advanced Adsorption, *Angew. Chem., Int. Ed.*, 2003, **42**, 3146–3150.
4 Y. H. Deng, D. W. Qi, C. H. Deng, X. M. Zhang and D. Y. Zhao, Superparamagnetic High-Magnetization Microspheres with an Fe_3O_4@SiO_2 Core and Perpendicularly Aligned Mesoporous SiO_2 Shell for Removal of Microcystins, *J. Am. Chem. Soc.*, 2008, **130**, 28–29.
5 Y. H. Deng, Y. Cai, Z. K. Sun, J. Liu and D. Y. Zhao, Multifunctional Mesoporous Composite Microspheres with Well-Designed Nanostructure: A Highly Integrated Catalyst System, *J. Am. Chem. Soc.*, 2010, **132**, 8466–8473.
6 T. Wagner, S. Haffer, C. Weinberger, D. Klaus and M. Tiemann, Mesoporous Materials as Gas Sensors, *Chem. Soc. Rev.*, 2013, **42**, 4036–4053.
7 Z. K. Sun, Y. H. Deng, J. Wei, D. Gu, B. Tu and D. Y. Zhao, Hierarchically Ordered Macro-/Mesoporous Silica Monolith: Tuning Macropore Entrance Size for Size-Selective Adsorption of Proteins, *Chem. Mater.*, 2011, **23**, 2176–2184.
8 H. F. Yang, Q. H. Shi, B. Z. Tian, S. H. Xie and D. Y. Zhao, A Fast Way for Preparing Crack-Free Mesostructured Silica Monolith, *Chem. Mater.*, 2003, **15**, 536–541.
9 F. C. Leinweber, D. Lubda, K. Cabrera and U. Tallarek, Characterization of Silica-Based Monoliths with Bimodal Pore Size Distribution, *Anal. Chem.*, 2002, **74**, 2470–2477.
10 K. Nakanishi, Y. Kobayashi, T. Amatani, K. Hirao and T. Kodaira, Spontaneous Formation of Hierarchical Macro-Mesoporous Ethane–Silica Monolith, *Chem. Mater.*, 2004, **16**, 3652–3658.
11 J. Smått, S. Schunk and M. Lindén, Versatile Double-Templating Synthesis Route to Silica Monoliths Exhibiting a Multimodal Hierarchical Porosity, *Chem. Mater.*, 2003, **15**, 2354–2361.
12 S. C. Park, T. Ito and D. A. Higgins, Single Molecule Tracking Studies of Flow-Aligned Mesoporous Silica Monoliths: Aging-Time Dependence of Pore Order, *J. Phys. Chem. B*, 2013, **117**, 4222–4230.
13 N. A. Melosh, P. Lipic, F. S. Bates and B. F. Chmelka, Molecular and Mesoscopic Structures of Transparent Block Copolymer-Silica Monoliths, *Macromolecules*, 1999, **32**, 4332–4342.
14 B. J. Scott, G. Wirnsberger and G. D. Stucky, Mesoporous and Mesostructured Materials for Optical Applications, *Chem. Mater.*, 2001, **13**, 3140–3150.
15 C. F. Xue, J. X. Wang, B. Tu and D. Y. Zhao, Hierarchically Porous Silica with Ordered Mesostructure from Confinement Self-Assembly in Skeleton Scaffolds, *Chem. Mater.*, 2010, **22**, 494–503.
16 Q. Li, Z. X. Wu, D. Feng, B. Tu and D. Y. Zhao, Hydrothermal Stability of Mesostructured Cellular Silica Foams, *J. Phys. Chem. C*, 2010, **114**, 5012–5019.
17 V. Meynen, P. Cool and E. F. Vansant, Verified Synthesis of Mesoporous Materials, *Microporous Mesoporous Mater.*, 2009, **125**, 170–223.
18 M. B. Bryning, D. E. Milkie, M. F. Islam, L. A. Hough and A. G. Yodh, Carbon Nanotube Aerogels, *Adv. Mater.*, 2007, **19**, 661–664.
19 Y. Zhao, J. Liu, Y. Hu, H. H. Cheng, A. Y. Cao and L. T. Qu, Highly Compression-Tolerant Supercapacitor Based on Polypyrrole-mediated Graphene Foam Electrodes, *Adv. Mater.*, 2013, **25**, 591–595.
20 X. C. Gui, J. Q. Wei, K. L. Wang, A. Y. Cao, H. W. Zhu and D. H. Wu, Carbon Nanotube Sponges, *Adv. Mater.*, 2010, **22**, 617–621.

21 K. H. Kim, Y. Oh and M. F. Islam, Graphene Coating Makes Carbon Nanotube Aerogels Superelastic and Resistant to Fatigue, *Nat. Nanotechnol.*, 2012, **7**, 562–566.
22 S. Nardecchia, D. Carriazo, M. L. Ferrer, M. C. Gutierrez and F. del Monte, Three Dimensional Macroporous Architectures and Aerogels Built of Carbon Nanotubes and/or Graphene: Synthesis and Applications, *Chem. Soc. Rev.*, 2013, **42**, 794–830.
23 H. Hu, Z. B. Zhao, W. B. Wan, Y. Gogotsi and J. S. Qiu, Ultralight and Highly Compressible Graphene Aerogels, *Adv. Mater.*, 2013, **25**, 2219–2223.
24 J. H. Zou, J. H. Liu, A. S. Karakoti, A. Kumar, D. Joung, Q. Li, S. I. Khondaker, S. Seal and L. Zhai, Ultralight Multiwalled Carbon Nanotube Aerogel, *ACS Nano*, 2010, **4**, 7293–7302.
25 Z. Xu, Y. Zhang, P. G. Li and C. Gao, Strong, Conductive, Lightweight, Neat Graphene Aerogel Fibers with Aligned Pores, *ACS Nano*, 2012, **6**, 7103–7113.
26 Z.-S. Wu, Y. Sun, Y.-Z. Tan, S. B. Yang, X. L. Feng and K. Müllen, Three-Dimensional Graphene-Based Macro- and Mesoporous Frameworks for High-Performance Electrochemical Capacitive Energy Storage, *J. Am. Chem. Soc.*, 2012, **134**, 19532–19535.
27 H. Huang, P. W. Chen, X. T. Zhang, Y. Lu and W. C. Zhan, Edge-to-Edge Assembled Graphene Oxide Aerogels with Outstanding Mechanical Performance and Superhigh Chemical Activity, *Small*, 2013, **9**, 1397–1404.
28 W. F. Chen, S. R. Li, C. H. Chen and L. F. Yan, Self-Assembly and Embedding of Nanoparticles by In Situ Reduced Graphene for Preparation of a 3D Graphene/Nanoparticle Aerogel, *Adv. Mater.*, 2011, **23**, 5679–5683.
29 M. A. Worsley, P. J. Pauzauskie, T. Y. Olson, J. Biener, J. H. Satcher, Jr and T. F. Baumann, *J. Am. Chem. Soc.*, 2010, **132**, 14067–14069.
30 H. P. Cong, X. C. Ren, P. Wang and S. H. Yu, Macroscopic Multifunctional Graphene-Based Hydrogels and Aerogels by a Metal Ion Induced Self-Assembly Process, *ACS Nano*, 2012, **6**, 2693–2703.
31 K. L. Ding, B. J. Hu, Y. Xie, G. M. An and Z. M. Liu, A Simple Route to Coat Mesoporous SiO_2 Layer on Carbon Nanotubes, *J. Mater. Chem.*, 2009, **19**, 3725–3731.
32 M. Zhang, Y. P. Wu, X. Z. Feng, L. X. Chen and Y. K. Zhang, Fabrication of Mesoporous Silica-Coated CNTs and Application in Size-Selective Protein Separation, *J. Mater. Chem.*, 2010, **20**, 5835–5842.
33 X. H. Lu, H. Q. Liu, C. H. Deng and X. M. Yan, Facile Synthesis and Application of Mesoporous Silica Coated Magnetic Carbon Nanotubes, *Chem. Commun.*, 2011, **47**, 1210–1212.
34 X. F. Qian, Y. Y. Lv, W. Li, Y. Y. Xia and D. Y. Zhao, Multiwall Carbon Nanotube@Mesoporous Carbon with Core-Shell Configuration: a Well-Designed Composite-Structure toward Electrochemical Capacitor Application, *J. Mater. Chem.*, 2011, **21**, 13025–13031.